iScience

CellPress
OPEN ACCESS

Article

Remarkable bactericidal traits of a metal-ceramic composite coating elated by hierarchically structured surface

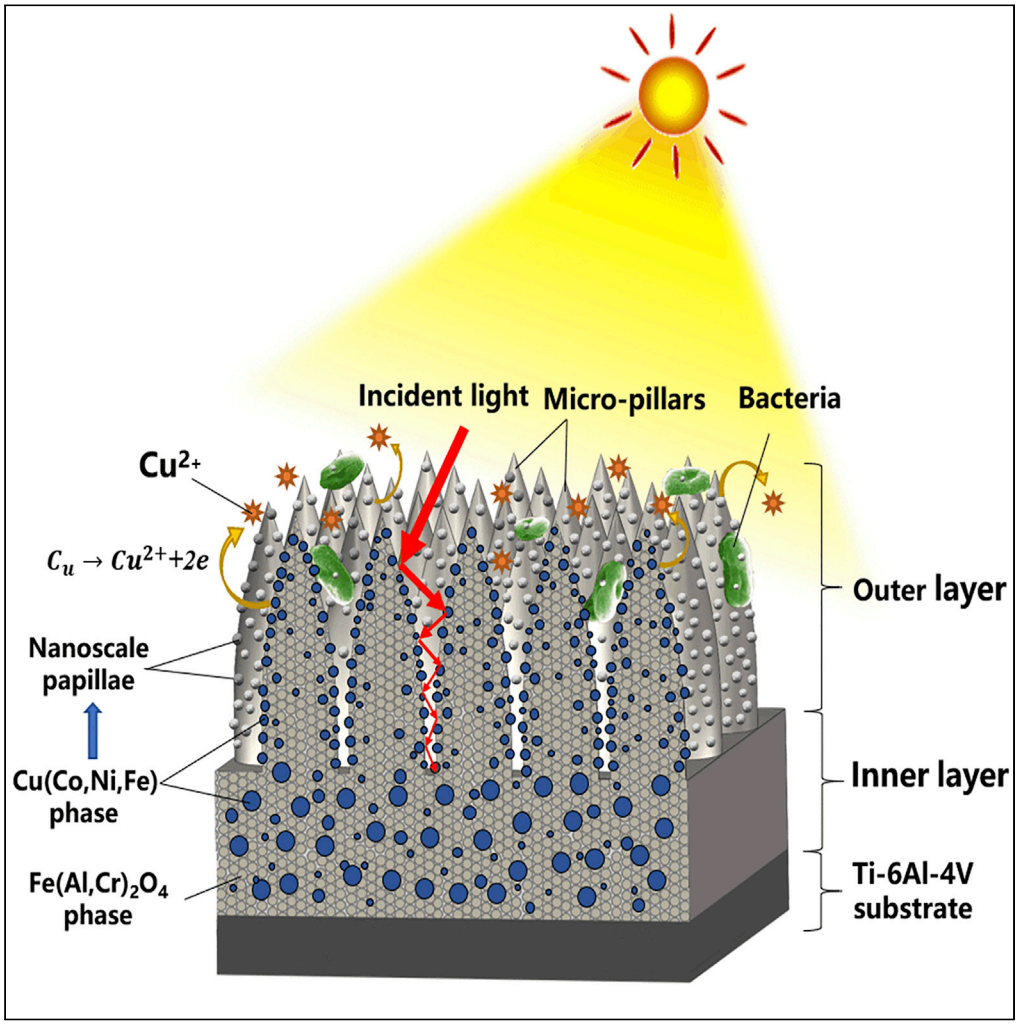

Jiang Xu, Zhijian Pan, Shaung Peng, ..., Yu jie Chen, Zong-Han Xie, Paul Munroe

xujiang73@nuaa.edu.cn

Highlights

The coating exhibits a hierarchical surface structure

The coating possesses adhesive superhydrophobicity

The coating shows a strong light harvesting capability over a broad wavelength

The coating offers three distinct pathways for combating the bacterial infection

Xu et al., iScience *24*, 101942
January 22, 2021
https://doi.org/10.1016/j.isci.2020.101942

iScience

CellPress
OPEN ACCESS

Article

Remarkable bactericidal traits of a metal-ceramic composite coating elated by hierarchically structured surface

Jiang Xu,[1,5,*] Zhijian Pan,[1] Shaung Peng,[1] Yanjie Zhao,[1] Shuyun Jiang,[2] Yu jie Chen,[3] Zong-Han Xie,[3] and Paul Munroe[4]

Summary

A ceramic-based coating with a hierarchical surface structure was synthesized via solid-state reaction enabled by a double cathode glow discharge technique. This innovative coating comprises two distinct layers, specifically an outer layer with a well-aligned micro-pillar array and a dense inner layer. Both are composed of a face-centered cubic Cu(Co,Ni,Fe) solid solution phase together with a spinel-type $Fe(Al,Cr)_2O_4$ oxide. This coating exhibits superhydrophobicity and, yet, a very strong adhesion to water, i.e., the so-called "rose petal effect". This coating also exhibits highly efficient antibacterial ability against both *Staphylococcus aureus* and *Escherichia coli* bacteria under both dark and visible light conditions. The excellent antibacterial property originates from the synergistic effects through the release of Cu ions coupled with photothermal activity upon light activation.

Introduction

Diseases caused by pathogenic microbial infections pose a global health threat because the multi-drug resistance of some emerging bacterial strains has rendered conventional antibiotic therapies ineffective (Campoccia et al., 2006). The rapid development of bacterial antibiotic resistance has been expedited by the life cycle of the microorganism (Cheeseman et al., 2020). Bacterial infections stem mainly from microbial adhesion, colonization, and subsequent bacterial biofilm formation, which act as reservoirs for bacteria and are difficult to obliterate through antimicrobial agents due to the protective barrier effect provided by the self-produced extracellular polymeric matrices (Elbourne et al., 2019a). Bacterial infections are inextricably bound to the transmission of nosocomial pathogenic microbes from contaminated surfaces and medical devices to healthy patients. Therefore, it is necessary to explore innovative alternative antimicrobial avenues to combat the shortcomings of drug resistance to antibiotics and so reduce hospital-acquired infections.

Attempts have been made to develop materials that are able to exhibit long-lasting, highly efficient, and broad-spectrum antibacterial activity without provoking antimicrobial resistance (Anandhan et al., 2019; Adlhart et al., 2018). Since the surface properties of a material have an important influence on initial adhesion and growth of bacterial strains on its surface, a variety of micro-/nano-patterned hierarchical surfaces have been explored, with the objective of improving antibacterial properties. These antimicrobial strategies rely on introducing and/or improving a number of surface functions, such as mitigating bacterial attachment by superhydrophobic effects (Qian and Cheng, 2018; Li et al., 2017), mechanical damage of bacterial cell walls while in contact with microstructured/nanostructured surfaces (Elbourne et al., 2019b, 2020; Dunseath et al., 2019; Ivanova et al., 2020), and photothermal impacts activated upon light illumination (Wu et al., 2013; Liu et al., 2018). Such effects are predominantly determined by the surface topography and the type of microbial species.

Unlike pure metal oxides that have poor photocatalyst properties, transition metal-based spinel oxides are a special class of compounds that have attracted considerable interest because of their remarkable photocatalytic behavior, high chemical activity, and magnetic properties (Barakat et al., 2008; Tavares et al., 1999). In particular, spinel-structured black metal oxides have enormous potential as solar absorbing coatings for applications in solar thermal plants (de Arrieta et al., 2019). Therefore, these spinel oxides are

[1]Department of Material Science and Engineering, Nanjing University of Aeronautics and Astronautics, 29 Yudao Street, Nanjing 210016, PR China

[2]Department of Mechanical Engineering, Southeast University, 2 Si Pai Lou, Nanjing 210096, PR China

[3]School of Mechanical Engineering, University of Adelaide, Adelaide, SA 5005, Australia

[4]School of Materials Science and Engineering, University of New South Wales, Sydney, NSW 2052, Australia

[5]Lead contact

*Correspondence: xujiang73@nuaa.edu.cn

https://doi.org/10.1016/j.isci.2020.101942

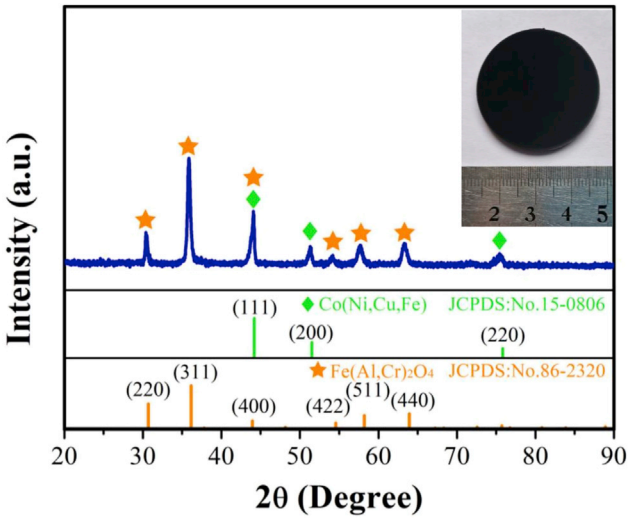

Figure 1. XRD pattern and macroscopic morphology of the as-received coating

XRD pattern recorded from the as-received coating and the upper inset shows the optical photographs of its macroscopic morphology.

envisaged to possess promising antibacterial properties endowed in part by their photothermal response activated by their capacity to absorb visible light. Nonetheless, to the authors' knowledge, there have been no studies on the utilization of spinel oxides, combined with micro-/nano-topographical surface features, to investigate their potential as photothermal antibacterial coatings. Bearing this in mind, we investigated the in vitro antibacterial activity of a Cu(Co,Ni)/Fe(Al,Cr)$_2$O$_4$ duplex phase coating against both *Staphylococcus aureus* (*S.aureus*) and *Escherichia coli* (*E. coli*) bacteria under both dark and visible light conditions, with a focus on the effect of the surface microstructural patterns and photothermal effects.

Results and discussion

Microstructural analysis

Figure 1 shows a representative X-ray diffraction (XRD) pattern of the coating, along with an optical photograph of its macroscopic morphology (inset in Figure 1). The diffraction lines from the coating arise from two distinct sets of reflections, which can be readily indexed to a face-centered cubic (*fcc*) structured Cu(Co,Ni,Fe) solid solution phase (JCPDS PDF#15–0806) and a Cr-substituted Fe(Al,Cr)$_2$O$_4$ spinel phase (JCPDS PDF # 86–2320), respectively. As compared to the standard powder diffraction file (PDF) data for FeAl$_2$O$_4$, the peak positions shift to lower 2θ angles, suggesting that the Al positions in the FeAl$_2$O$_4$ lattice are partially occupied by Cr, leading to an increase in lattice parameter due to the larger atomic radius of Cr. Relative percentages of the Fe(Al,Cr)$_2$O$_4$ and Cu(Co, Ni) phases in the coating were semi-quantitatively estimated using the reference intensity ratio method (Tobaldi et al., 2014). The relative concentrations of Fe(Al,Cr)$_2$O$_4$ and Cu(Co,Ni,Fe) phases were determined to be 68 wt% and 32 wt%, respectively. Combining the results of the XRD and scanning electron microscope-energy-dispersive spectrum (SEM-EDS) analysis, the in situ solid-state reaction during the sputtering deposition process might take place as follows:

$$4Fe_2O_3 + 6(Al,Cr) = 3Fe(Al,Cr)_2O_4 + 5Fe \quad \text{(Equation 1)}$$

From the inset in Figure 1, the entire surface of the specimen is uniformly covered with a black coating. Typical structural characteristics of the coating in both plan view and cross section are presented in Figures 2A–2D. From the SEM side view, the coating is composed of two distinct sublayers, specifically an outer layer consisting of bamboo-shoot-shaped micro-pillars and an inner layer with a compact structure. As shown in Figure 2A, these randomly aligned micro-pillars with an average height of about 14 μm grow in a direction perpendicular to the coating surface so as to produce a porous outer layer. The magnified view of this layer (Figure 2B) reveals that the surfaces of individual micro-pillars present with a dense array of nanoscale papillaes. Similar to the SEM analysis, these micro-pillars are clearly visible on the 3D surface topography of confocal microscopy shown in Figure 2C. The values for average surface roughness (S_a) and

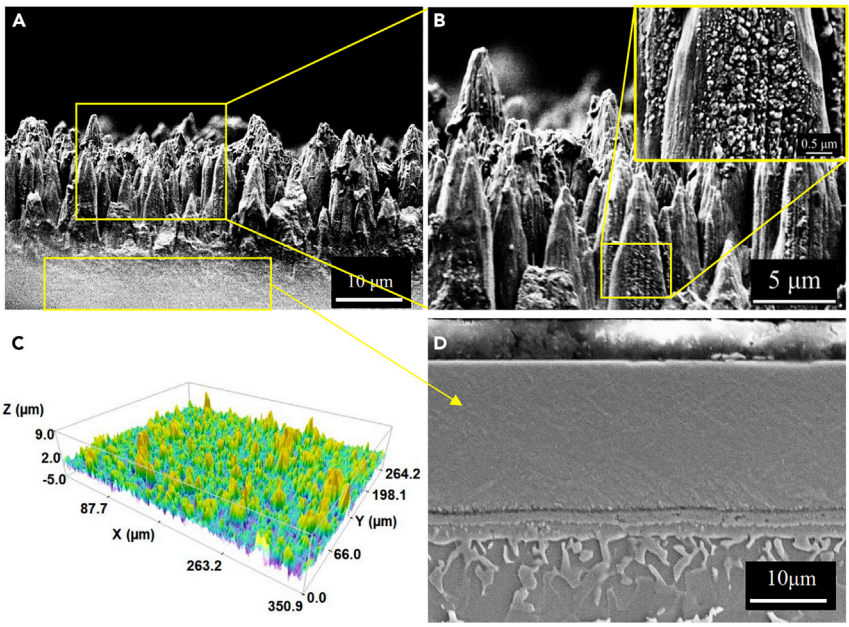

Figure 2. Typical structural characteristics

(A) Typical SEM side view of the outer layer of the coating, (B) high magnification image of the selected area in (A) and the upper inset in (B) show magnified view of individual micro-pillar, (C) 3D surface topography of confocal microscopy of the coating, (D) SEM image of the etched cross section of inner layer of the coating.

kurtosis (S_{ku}) recorded from a scan area of 350.9 μm × 264.2 μm were determined to be 1.008 μm and 7.650, respectively. The high S_{ku} value is closely related to the presence of conical head micro-pillars. Figure 2D presents a cross-sectional SEM image of the inner layer after complete removal of the outer layer through careful polishing. Unlike the outer layer, the inner layer, with an average thickness of ~19μm, exhibits uniform and compact structure together with a thin diffusion layer that may be beneficial to improve adhesion strength between the inner layer and the substrate. Figures 3A–3F shows Z-contrast high-angle annular dark-field scanning transmission electron microscopy (HAADF-STEM) cross-sectional micrographs taken from the outer layer of the coating. As shown in Figure 3A and the associated scanning transmission electron microscopy-energy-dispersive X-ray (STEM-EDX) elemental maps (see Figure S1 in the Supplementary materials), the Cu(Co,Ni,Fe) phase, which exhibits bright contrast, exists over a wide range of phase sizes from a few 10s of nm to a few hundred nanometers and appears to be embedded in an Al- and Cr-rich $Fe(Al,Cr)_2O_4$ matrix exhibiting dark contrast. STEM lattice images (Figures 3B and 3C) and corresponding fast Fourier transformation analysis (see insets) indicate that the bright phase and dark phase can be identified as *fcc*-structure Cu(Co,Ni,Fe) and a spinel-type $Fe(Al,Cr)_2O_4$ oxide, respectively. According to the HAADF-STEM analysis, it is suggested that these nanoscale papillaes, grown on the outside of the micro-pillars, are the Cu(Co,Ni,Fe) phase. Furthermore, as shown in Figures 3D–3F, the phase composition of the inner layer is also a mixture of Cu(Co,Ni,Fe) and $Fe(Al,Cr)_2O_4$ similar to the outer layer of the coating apart from particles of the Cu(Co,Ni,Fe) phase appearing larger in the inner layer. The presence of these similar two-phase structures in both the inner and outer layers was also verified by nano-indentation tests, as shown in Figure S2. The hardness (H) and elastic modulus (E) for the outer layer of the coating were determined to be 18.9 ± 1.3 GPa and 187.1 ± 6.1 GPa, respectively, which are comparable values to those for the inner layer of the coating (H = 18.1 ± 1.0, E = 181.6 ± 3.3). Similarity in the mechanical properties between the outer layer and the inner layer is consistent with their similar phase composition.

Water contact angle and photoabsorption properties

Figure 4 shows the contact angle that water droplets made on the as-received coating, the polished coating after removal of the outer layer, and the bare Ti-6Al-4V substrate. As can be seen from Figure 4, at a 0° tilt angle, the static contact angle increased from 64.1° for the substrate to 103.4° after coated with the polished inner layer and further rose to 151.5° after deposition of the as-prepared coating. Interestingly, the water droplet on the as-prepared coating clings to the coating surface and still exhibits a

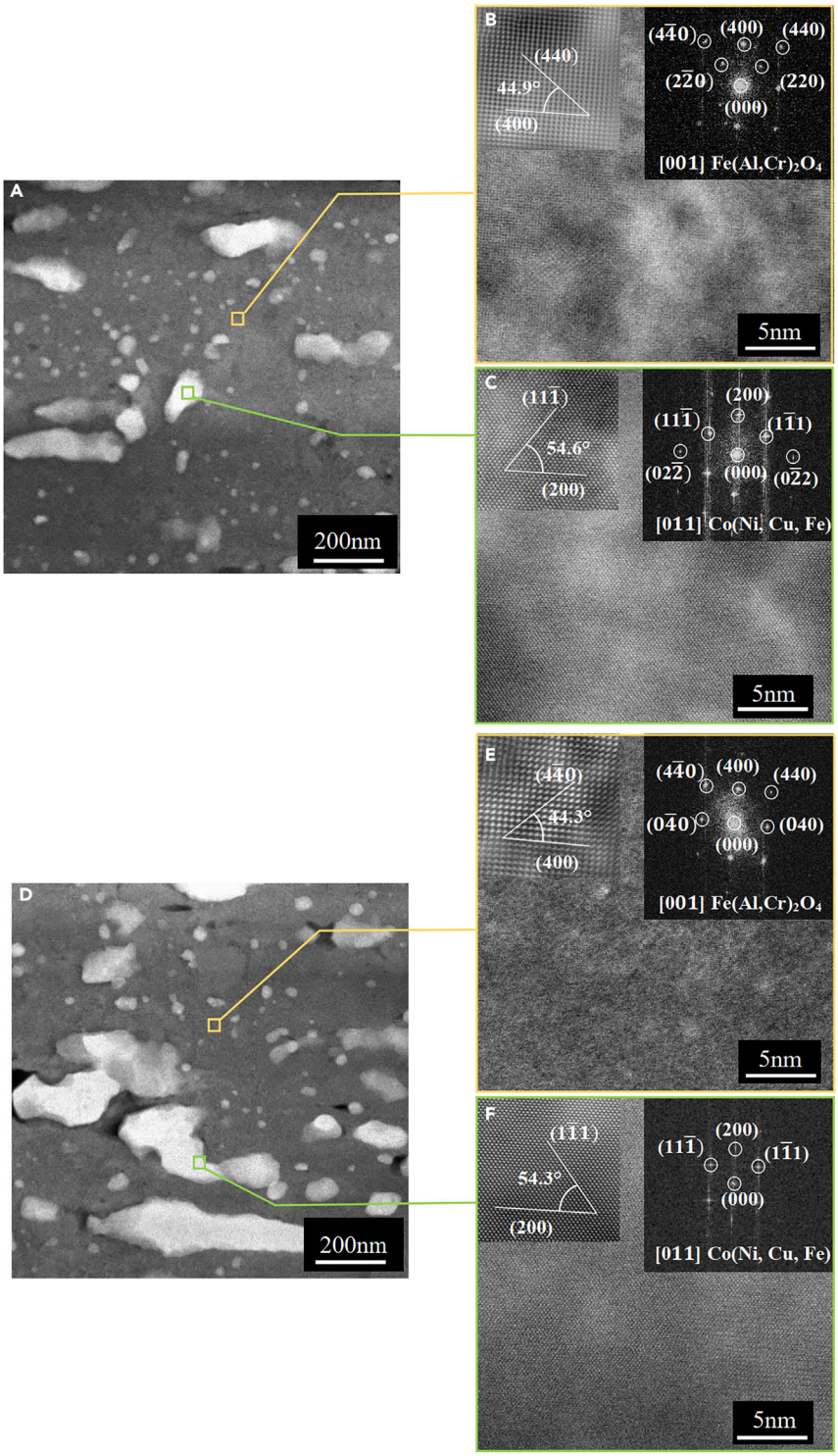

Figure 3. Phase and microstructure analysis

(A) Cross-sectional Z-contrast HAADF-STEM images and (B) STEM lattice images of $Fe(Al,Cr)_2O_4$ phase and (C) Cu(Co,Ni,Fe) phase taken from the outer layer of the coating. The insets in (B) and (C) show the corresponding fast Fourier transformation (FFT) images.

(D) Cross-sectional Z-contrast HAADF-STEM images and (E) STEM lattice images of $Fe(Al,Cr)_2O_4$ and (F) Cu(Co,Ni,Fe) phase taken from the inner layer of the coating. The insets in (E) and (F) show the corresponding fast Fourier transformation (FFT) images.

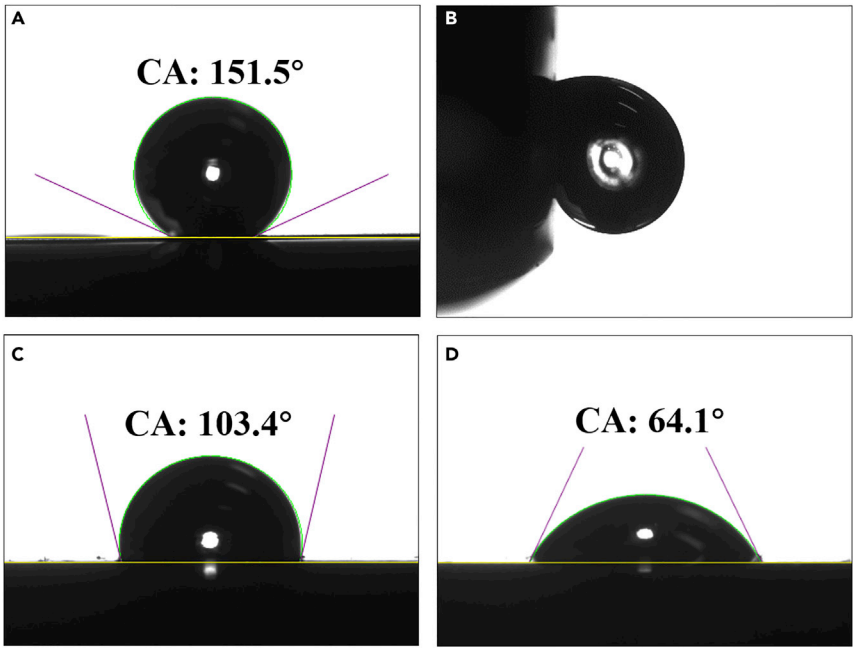

Figure 4. Water contact angle

Shapes of water droplets on the tested samples: the as-deposited coating with different tilt angles, (A) 0° and (B) 90°; (C) the polished coating and (D) uncoated Ti-6Al-4V substrate.

spherical shape even when the coating surface is tilted at 90° angle, suggesting that the as-prepared coating exhibits an apparent superhydrophobic adhesive property. Although both the inner layer and the outer layer have the same phase composition, the polished inner layer possesses less hydrophobicity, but the outer layer exhibits an adhesive superhydrophobicity. This special wetting property of the coating results from its hierarchical microscale/nanoscale surface configuration. Such a phenomenon, often termed the Cassie impregnating wetting state, has been observed on rose petals and is also called the "red rose petal effect" (Chang et al., 2009). The distance between two micro-pillars (average distance of about 5 μm) is so large that a water droplet can impregnate the gaps among these micro-pillars, such that the coating surface shows a high adhesive force to water due to the pinning of the water droplet by the coating at the contact line of three phases (specifically, water, the coating surface, and air). Meanwhile, the presence of air trapped among the nanoscale papillaes distributed on the micro-pillar surface can impede the penetration of the water into these nano-papillaes, which is responsible for the surface superhydrophobicity of the coating (Feng et al., 2008).

To ascertain the influence of surface morphology of the as-prepared coating on its photoabsorption properties, the absorption spectra of the as-deposited coating, the polished coating after removal of the outer layer, and the uncoated Ti-6Al-4V substrate were measured using a UV-vis-near-infrared (NIR) spectrophotometer, as displayed in Figure 5A. As compared to the polished coating and uncoated Ti-6Al-4V substrate, the outer as-deposited coating exhibits a much higher absorption over a broad wavelength range from 200 nm to 2.5 μm and shows near-perfect absorption (>95%) at wavelengths greater than 500 nm, consistent with the hierarchical micro-/nano-surface structure. This suggests effective light harvesting capability of the outer coating with an absorption band spanning from the visible light region to the NIR region. There are three reasons for the higher optical absorption for the coating with its hierarchical multi-scaled surface structure (Wattoo et al., 2018; Cui and Wardle, 2019; Yin et al., 2017): (1) bamboo-shoot-shaped micro-pillars with conical tops provide a graded refractive index and can match well with the incident light restricting unwanted Fresnel reflections; (2) the large and deep pores induced by the presence of bamboo-shoot-shaped micro-pillars act as optical cavities to obtain high efficient light trapping; and (3) owing to the presence of nano-papillaes, the incoming light trapped between the micro-pillars undergoes multiple internal reflections and scatterings, thereby providing enhanced light absorption by extending the light path. In addition, according to the absorption spectrum of the polished coating, the dense inner layer also contributes to the light absorbing over almost the entire wavelength range investigated and thus decreases the

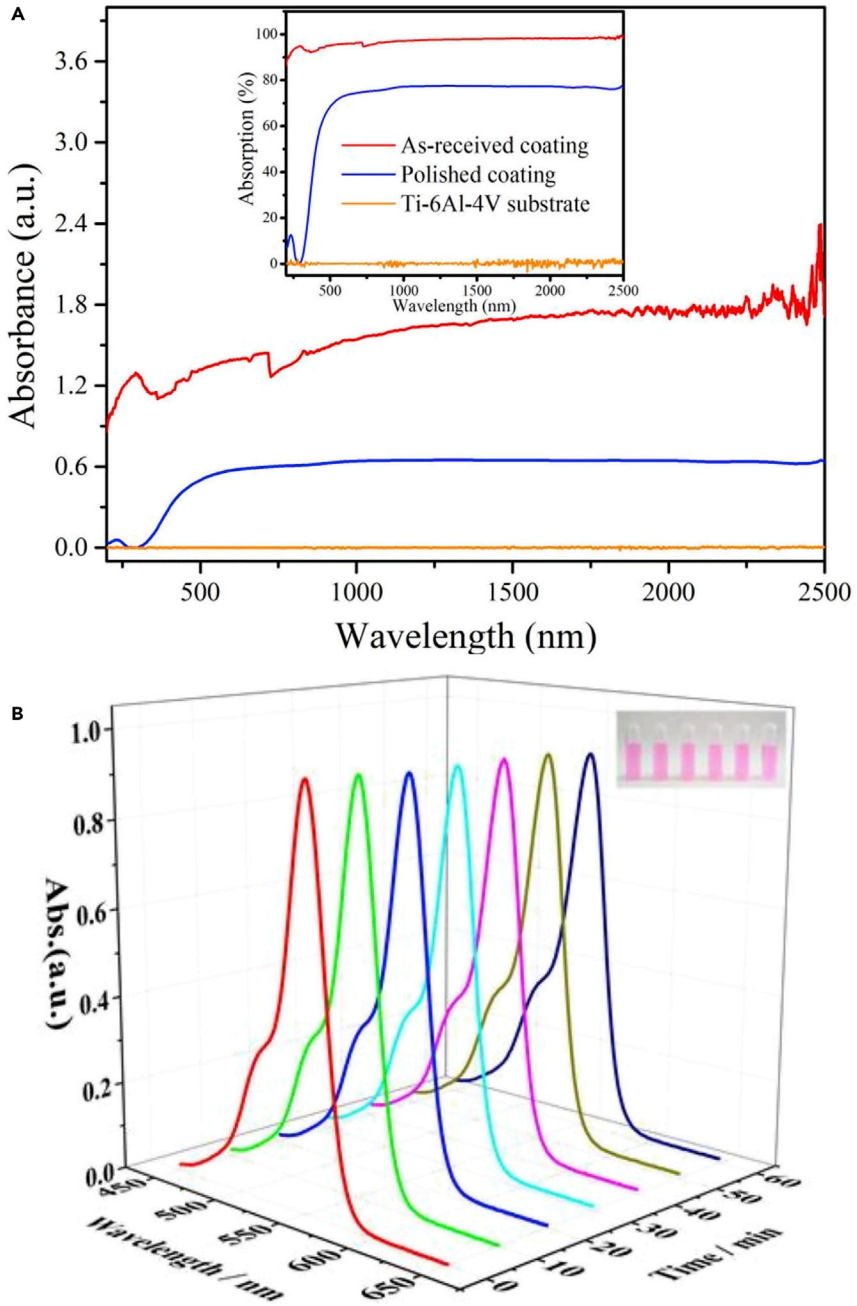

Figure 5. Photoabsorption properties

(A) The absorbance and the absorption spectra (inset in [A]) of the as-deposited coating, the polished coating, and uncoated Ti-6Al-4V substrate.

(B) The intensity of the absorption peak for RhB dye solution after different times under visible light (>420 nm) irradiation.

reflectance of the outer layer. Figure S3 presents the temperature of the bacteria solution as a function of light irradiation time, where samples with dimensions of 10 mm × 10 mm × 0.2 mm were immersed in 30 mL of bacteria solution. After light irradiation for 20 min, the temperature of the bacteria solution for the outer as-deposited coating and the polished inner coating rose quickly from room temperature to 58.3°C and 42.7°C, respectively, while the temperature of the bacteria solution for Ti-6Al-4V substrate only rose slightly (2.4°C) from room temperature. This suggests that the coating offers superior photothermal activation to convert the absorbed visible light energy into heat energy. The photocatalytic activities of

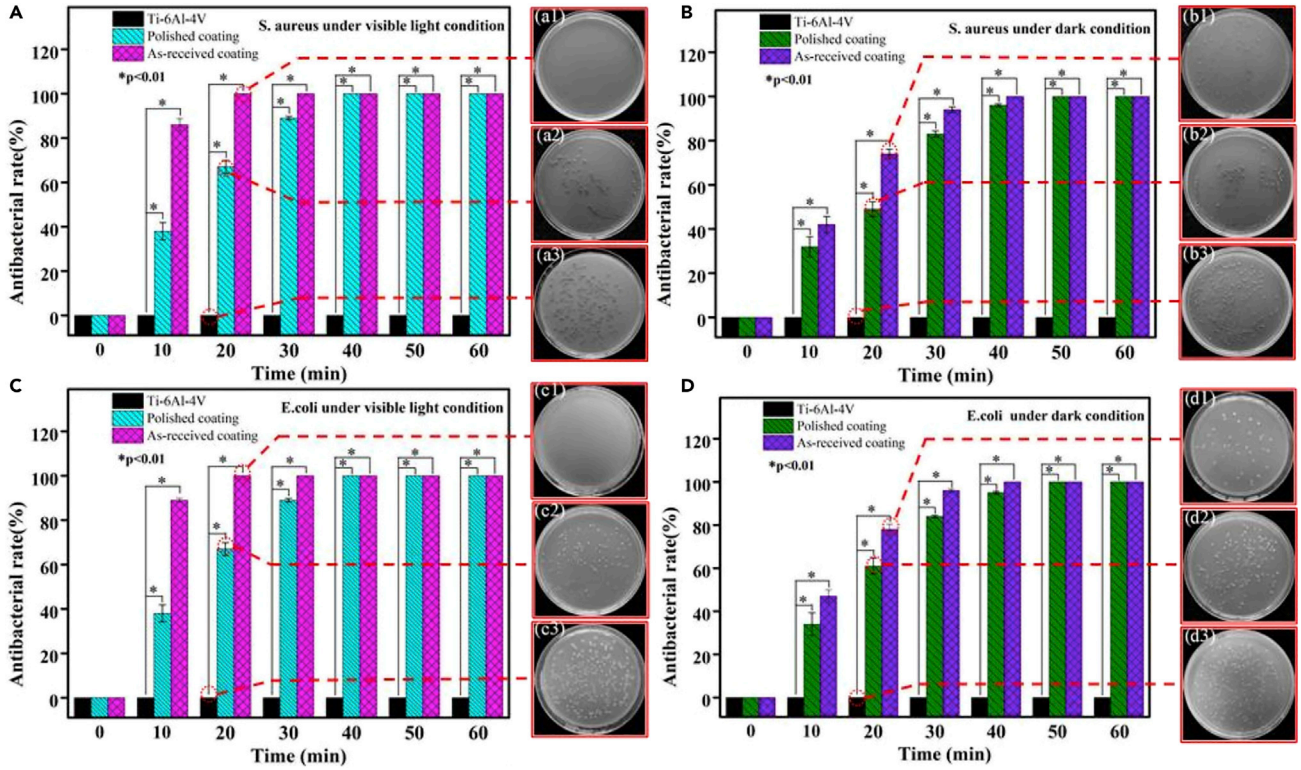

Figure 6. Antibacterial activity

The antibacterial rate of the as-deposited coating, the polished coating, and uncoated Ti-6Al-4V substrate against *S. aureus* (A and B) and *E. coli* (C and D), under both visible light (A and C) and dark (B and D) conditions. Photographs of bacterial colonies grown on LB agar plates inoculated with *S. aureus* and *E. coli* after 20 min exposure with or without light irradiation.

the coating were studied by monitoring the degradation of rhodamine B (RhB) dye solution under visible light irradiation (>420 nm), as presented in Figure 5B. Clearly, after 60 min irradiation, no change in the intensity of the absorption peak for RhB dye solution at 554 nm was observed, and the color of the dye remained unchanged (inset in Figure 5B). This means that the coating is unable to photodegrade RhB dye molecule, denoting a lack of photocatalytic activity.

Antibacterial activity

Figure 6 shows the antibacterial efficiencies of the coating, the polished coating, and bare Ti-6Al-4V substrate against *S. aureus* and *E. coli* under both dark and visible light conditions, together with the photographs of the number of bacterial colonies formed by each of the bacteria. Under dark condition, the as-deposited coating and the polished coating exhibited no significant difference in antibacterial effect, but the time taken to kill all the bacteria was shorter for the as-deposited coating than the polished coating. Nevertheless, after 20 min of light irradiation exposure, almost no *E. coli* or *S. aureus* colonies for the as-deposited coating were detected on the agar disc, meaning that almost 100% of the bacteria were killed by the as-deposited coating, whereas the polished coating showed a 60–70% sterilization efficiency under the same condition. Both of which are higher than the values obtained in the absence of irradiated light. Whether under dark or visible light, large numbers of bacterial colonies on bare Ti-6Al-4V remain almost unchanged, indicating that bare Ti-6Al-4V has no any bacteriostatic effect on the two bacteria investigated.

Generally speaking, the bactericidal properties of Cu-containing materials depend largely on the release of dissolved Cu^{2+} cations. The positively charged Cu^{2+} cations can adhere to the negatively charged cell wall of a bacterium through electrostatic interactions, leading to several effects, including inhibition of the function of enzymes and the normal respiratory functions of bacteria, destruction of bacterial membrane integrity, and a hindering of the replication of DNA molecules (Burghardt et al., 2015; Matsumoto et al., 2009; Ekthammathat et al., 2016). Because the presence of the nanoscale Cu(Co,Ni,Fe) phase

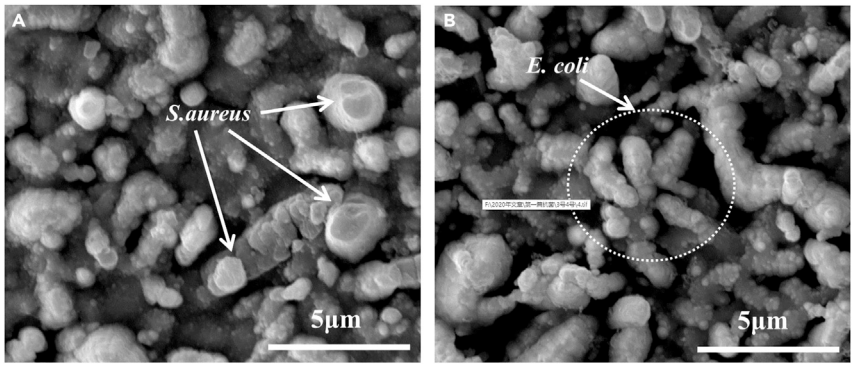

Figure 7. Morphology of bacteria
SEM images of bacterial cells of *S. aureus* (A) and *E. coli* (B) after 1h exposed to as-deposited coating.

significantly enhances the surface to volume ratio, both the as-deposited coating and the polished coating leach metal ions at a much higher rate, compared with their coarse-grained counterparts (Cheeseman et al., 2020). Therefore, for the as-deposited coating and the polished coating, the Cu^{2+} cations effectively kill both bacterial strains without irradiation. The inductively-coupled plasma mass spectroscopy (ICP-MS) results indicate that the amounts of released Cu^{2+} ions are 0.02 and 0.14 ppm, respectively. In addtion, the Cu ion release tests are also performed under visible light irradiation. The results indicate that lighting irradiation has no effect on the release of Cu^{2+} ions. Compared with the polished coating, the as-deposited coating with rougher surface greatly increases the surface area in close contact with bacterial suspension, and hence, more Cu^{2+} cations are released into the environment, enhancing its antibacterial properties. Furthermore, the array of the nano-papillae, being 30–70 nm in diameter and spaced 80 nm apart, is similar to the surface nanostructure arranged on the surface of cicada wings (Kelleher et al., 2016). Previous studies indicated that such a surface nano-architecture possessed physical bactericidal properties because the nano-papillae would exert the deformational stresses on the cell wall and inner membrane of bacterial strains that have adhered to their surface, leading to irreversible mechanical rupture of the cell membrane and eventual cell death (Elbourne et al., 2017). To determine whether or not there is any physicomechanical damage mechanism for the duplex phase coating, the cell morphologies of the two bacteria incubated for 1 hr on the as-prepared coating and uncoated Ti-6Al-4V were observed. As shown in Figure 7, many grooves and slight distort are evident on the cell wall of the two bacteria, indicating that the severe morphological and structural injuries occurred on cell membranes of the two bacteria. However, there is no evidence that the nano-patterned surface structure present on the coating has physically disrupted the bacteria upon attachment to its surface.

Overwhelming evidence has indicated that common pathogenic bacteria could be killed at ambient temperatures above 55°. At this temperature, enzymes are denatured, and lipids and proteins on the bacterial cell membrane are destroyed, resulting in bacterial cell death (Xu et al., 2019; Liang et al., 2019). Owing to its strong light-thermal conversion capabilities, the photothermal activation of the as-prepared coating, triggered by irradiation with visible light, releases a substantial amount of thermal heat and raises the temperature of the hot zone at the interface between the coating and bacteria solution, which engenders irreversible bacterial destruction by thermal inactivation effect. The bactericidal ability of the duplex phase coating is comparable to or even stronger than that of some nanomaterials with a photothermal conversion effect. For example, Wu et al. (Wu et al., 2013) investigated the photothermal antibacterial properties of the graphene-oxide-wrapped gold nanocluster surface-enhanced Raman scattering (SERS) tags upon NIR laser irradiation (785 nm, 0.4 W cm^{-2}). The results showed that the antibacterial rates of this nanomaterial reached 92.55% and 97.02% for *E. coli* and *S. aureus*, respectively. Suo et al. (Suo et al., 2018) reported that the antibacterial rates of LuVO4:Nd^{3+}/Yb^{3+}/E^{r3+}@SiO2@Cu2S against bacteria *E. coli* and *S. aureus* were 96.6% and 96.2%, respectively, after 808-nm laser irradiation. Compared with the coating reported here, some nanomaterials exhibited better photothermal antibacterial efficiency toward both *E. coli* and *S. aureus*, e.g., nearly complete bacteria killing for both the two bacteria after NIR irradiation of less than 10 min (Lin et al., 2014; Shao et al., 2018; Zhu et al., 2018). However, under dark condition, these photothermal antibacterial nanomaterials were almost harmless to bacterial growth of *E. coli* and *S. aureus*. In contrast, in our case, the release of Cu^{2+} cations can improve the bactericidal effect of the as-deposited coating without light irradiation. Therefore, the as-deposited coating exhibits a

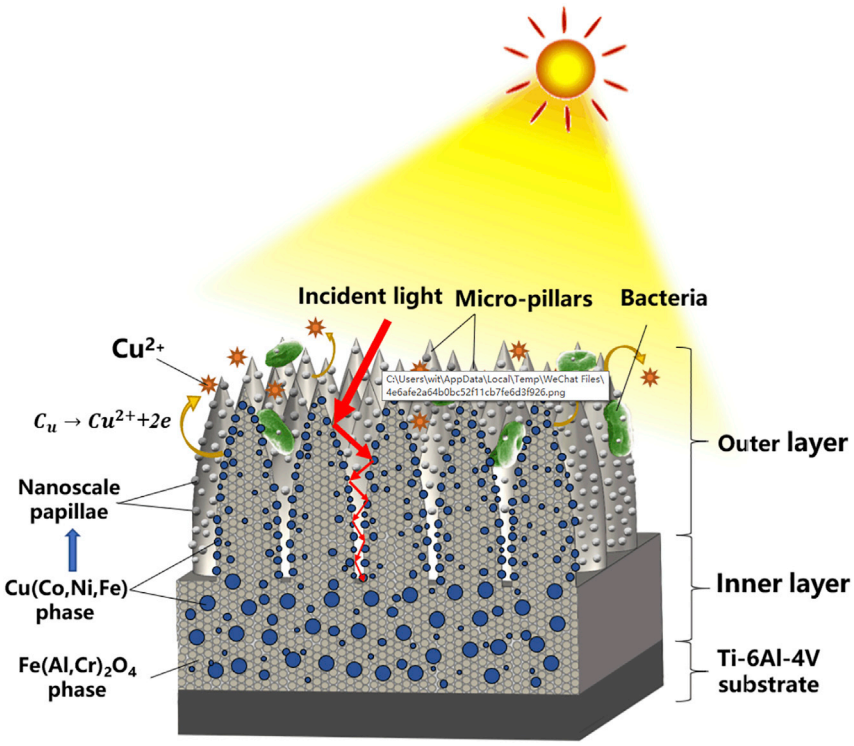

Figure 8. Antibacterial mechanisms of the coating

Schematic diagram illustrating the antibacterial mechanisms operating in the Cu(Co,Ni)/Fe(Al,Cr)2O4 duplex phase coating.

higher killing efficiency against both bacteria strains by synergistic action of several antibacterial mechanisms. The schematic diagrams illustrating the synergistic effects of several antibacterial mechanisms for the Cu(-Co,Ni)/$Fe(Al,Cr)_2O_4$ duplex phase coating are presented in Figure 8.

In conclusion, Cu(Co, Ni)/$Fe(Al,Cr)_2O_4$ duplex phase coating was fabricated using the double cathode glow discharge technique. The new coating consists of a porous outer layer and a dense inner layer. The outer layer exhibits a hierarchical micro-/nano-patterned surface architecture, where the bamboo-shoot-shaped micro-pillars are densely distributed and covered with nanoscale papillaes. The hierarchical surface topography endows the coating with an adhesive superhydrophobicity, an excellent light harvesting capability, and light-to-heat conversion ability. Antibacterial results suggest that the as-received coating shows rapid and effective bactericidal performances against both gram-negative (*E.coli*) and gram-positive bacteria (*S. aureus*) bacteria. Both strains are completely disinfected upon illumination with visible light for 20 min. The duplex phase coating offers a unique combination of multi-antibacterial mechanisms for combating microbial contamination, such as photothermal antibacterial activity and the release of Cu^{2+} cations. The hierarchical structured coating developed in this study offers an approach to the design of the broad-spectrum and high-efficiency antibacterial coating with the aid of synergistic sterilization strategies.

Limitations of the study

In this work, the ceramic-based coating was only prepared onto a Ti-6Al-4V substrate, and the coating substrate exhibits the compact form of bounding, free of any visible defects, because the difference in coefficients of thermal expansion between the coating and Ti-6Al-4V substrate may be neglected. However, if this coating is deposited on other metallic substrates, such as stainless steels, the coating may peel off, due to a large difference in coefficients of thermal expansion between the coating and substrate.

Methods

All methods can be found in the accompanying Transparent methods supplemental file.

Supplemental information

Supplemental information can be found online at https://doi.org/10.1016/j.isci.2020.101942.

Acknowledgments

The authors acknowledge the financial support of the General Program of the National Natural Science Foundation of China under Grant No. 52075245 and 51675267 and the Key Program of the National Natural Science Foundation of China under Grant No. 51635004.

Author contributions

Conceptualization, X.J.; Methodology, X.J.; Formal Analysis, P.S., S.J., Z.H., and P.M.; Investigation, Z.P. and Y. C.; Resources, X.J.; Writing – Original Draft, X.J.; Writing – Review & Editing, X.J., Z.H., and P.M.; Visualization, Z.P., P.S., and Y.Z.; Supervision, X.J.; Project Administration, X.J.; Funding Acquisition, X.J.

Declaration of interests

The authors declare no competing interests.

Received: August 1, 2020
Revised: November 15, 2020
Accepted: December 10, 2020
Published: January 22, 2021

References

Adlhart, C., Verran, J., Azevedo, N.F., Olmez, H., Keinänen-Toivola, M.M., Gouveia, I., Melo, L.F., and Crijns, F. (2018). Surface modifications for antimicrobial effects in the healthcare setting: a critical overview. J. Hosp. Infect. *99*, 239–249.

Anandhan, K., Harish, S., and Kumar, R.T. (2019). Effect of morphology on the formation of CdO nanostructures for Antibacterial and Hemolytic studies. Appl. Surf. Sci. *489*, 262–268.

Barakat, N.A.M., Khil, M.S., Sheikh, F.A., and Kim, H.Y. (2008). Synthesis and optical properties of two cobalt oxides (CoO and Co_3O_4) nanofibers produced by electrospinning process. J. Phys. Chem. C *112*, 12225–12233.

Burghardt, I., Lüthen, F., Prinz, C., Kreikemeyer, B., Zietz, C., Neumann, H.-G., and Rychly, J. (2015). A dual function of copper in designing regenerative implants. Biomaterials *44*, 36–44.

Campoccia, D., Montanaro, L., and Arciola, C.R. (2006). The significance of infection related to orthopedic devices and issues of antibiotic resistance. Biomaterials *27*, 2331–2339.

Chang, F.-M., Hong, S.-J., Sheng, Y.-J., and Tsao, H.-K. (2009). High contact angle hysteresis of superhydrophobic surfaces: hydrophobic defects. Appl. Phys. Lett. *95*, 064102.

Cheeseman, S., Christofferson, A.J., Kariuki, R., Cozzolino, D., and Elbourne, A. (2020). Antimicrobial metal nanomaterials: from passive to stimuli-activated applications. Adv. Sci. *7*, 1902913.

Cui, K., and Wardle, B.L. (2019). Breakdown of native oxide enables multifunctional, free-form carbon nanotube–metal hierarchical architectures. ACS Appl. Mater. Interfaces *11*, 35212–35220.

de Arrieta, I.G., Echániz, T., Fuente, R., Rubin, E., Chen, R., Igartua, J., Tello, M., and López, G. (2019). Infrared emissivity of copper-alloyed spinel black coatings for concentrated solar power systems. Sol. Energy Mater. Sol. Cells *200*, 109961.

Dunseath, O., Smith, E., Al-Jeda, T., Smith, J., King, S., May, P.W., Nobbs, A.H., Hazell, G., Welch, C.C., and Su, B. (2019). Studies of Black Diamond as an antibacterial surface for Gram Negative bacteria: the interplay between chemical and mechanical bactericidal activity. Sci. Rep. *9*, 1–10.

Ekthammathat, N., Phuruangrat, A., Thongtem, T., and Thongtem, S. (2016). Synthesis and characterization of Ce-doped CuO nanostructures and their photocatalytic activities. Mater. Lett. *167*, 266–269.

Elbourne, A., Chapman, J., Gelmi, A., Cozzolino, D., Crawford, R.J., and Truong, V.K. (2019a). Bacterial-nanostructure interactions: the role of cell elasticity and adhesion forces. J. Colloid Interface Sci. *546*, 192–210.

Elbourne, A., Cheeseman, S., Wainer, P., Kim, J., and Gaspera, E.D. (2020). Significant enhancement of antimicrobial activity in oxygen-deficient zinc oxide nanowires. ACS Appl. Bio Mater. *3*, 2997–3004.

Elbourne, A., Coyle, V.E., Truong, V.K., Sabri, Y.M., Kandjani, A.E., Bhargava, S.K., Ivanova, E.P., and Crawford, R.J. (2019b). Multi-directional electrodeposited gold nanospikes for antibacterial surface applications. Nanoscale Adv. *1*, 203–212.

Elbourne, A., Crawford, R.J., and Ivanova, E.P. (2017). Nano-structured antimicrobial surfaces: from nature to synthetic analogues. J. Colloid Interface Sci. *508*, 603–616.

Feng, L., Zhang, Y., Xi, J., Zhu, Y., Wang, N., Xia, F., and Jiang, L. (2008). Petal effect: a superhydrophobic state with high adhesive force. Langmuir *24*, 4114–4119.

Ivanova, E.P., Linklater, D.P., Werner, M., Baulin, V.A., Xu, X., Vrancken, N., Rubanov, S., Hanssen, E., Wandiyanto, J., and Truong, V.K. (2020). The multi-faceted mechano-bactericidal mechanism of nanostructured surfaces. Proc. Natl. Acad. Sci. U S A *117*, 12598–12605.

Kelleher, S.M., Habimana, O., Lawler, J., O'reilly, B., Daniels, S., Casey, E., and Cowley, A. (2016). Cicada wing surface topography: an investigation into the bactericidal properties of nanostructural features. ACS Appl. Mater. Interfaces *8*, 14966–14974.

Li, S., Huang, J., Chen, Z., Chen, G., and Lai, Y. (2017). A review on special wettability textiles: theoretical models, fabrication technologies and multifunctional applications. J. Mater. Chem. A *5*, 31–55.

Liang, Y., Zhao, X., Hu, T., Chen, B., Yin, Z., Ma, P.X., and Guo, B. (2019). Adhesive hemostatic conducting injectable composite hydrogels with sustained drug release and photothermal antibacterial activity to promote full-thickness skin regeneration during wound healing. Small *15*, 1900046.

Lin, D., Qin, T., Wang, Y., Sun, X., and Chen, L. (2014). Graphene oxide wrapped SERS tags: multifunctional platforms toward optical labeling, photothermal ablation of bacteria, and the monitoring of killing effect. ACS Appl. Mater. Interfaces *6*, 1320–1329.

Liu, R., Wang, X., Ye, J., Xue, X., Zhang, F., Zhang, H., Hou, X., Liu, X., and Zhang, Y. (2018). Enhanced antibacterial activity of silver-decorated sandwich-like mesoporous silica/reduced graphene oxide nanosheets through

photothermal effect. Nanotechnology *29*, 105704.

Matsumoto, N., Sato, K., Yoshida, K., Hashimoto, K., and Toda, Y. (2009). Preparation and characterization of β-tricalcium phosphate co-doped with monovalent and divalent antibacterial metal ions. Acta Biomater. *5*, 3157–3164.

Qian, S., and Cheng, Y.F. (2018). Fabrication of micro/nanostructured superhydrophobic ZnO-alkylamine composite films on steel for high-performance self-cleaning and anti-adhesion of bacteria. Colloids Surf. Physicochem. Eng. Aspects *544*, 35–43.

Shao, J., Ruan, C., Xie, H., Li, Z., Wang, H., Chu, P.K., and Yu, X.-F. (2018). Black-phosphorus-incorporated hydrogel as a sprayable and biodegradable photothermal platform for postsurgical treatment of cancer. Adv. Sci. *5*, 1700848.

Suo, H., Zhao, X., Zhang, Z., Wu, Y., and Guo, C. (2018). Upconverting $LuVO_4$: $Nd^{3+}/Yb^{3+}/Er^{3+}$@ SiO_2@ Cu_2S Hollow nanoplatforms for self-monitored photothermal ablation. ACS Appl. Mater. Interfaces *10*, 39912–39920.

Tavares, A.C., Cartaxo, M.A.M., Da Silva Pereira, M.I., and Costa, F.M. (1999). Effect of the partial replacement of Ni or Co by Cu on the electrocatalytic activity of the $NiCo_2O_4$ spinel oxide. J. Electroanal. Chem. *464*, 187–197.

Tobaldi, D.M., Pullar, R.C., Seabra, M.P., and Labrincha, J. (2014). Fully quantitative X-ray characterisation of evonik aeroxide TiO_2 P25®. Mater. Lett. *122*, 345–347.

Wattoo, A.G., Bagheri, R., Ding, X., Zheng, B., Liu, J., Xu, C., Yang, L., and Song, Z. (2018). Template free growth of robustly stable nanophotonic structures: broadband light superabsorbers. J. Mater. Chem. C *6*, 8646–8662.

Wu, M.C., Deokar, A.R., Liao, J.-H., Shih, P.-Y., and Ling, Y.-C. (2013). Graphene-based photothermal agent for rapid and effective killing of bacteria. ACS Nano *7*, 1281–1290.

Xu, J.-W., Yao, K., and Xu, Z.-K. (2019). Nanomaterials with a photothermal effect for antibacterial activities: an overview. Nanoscale *11*, 8680–8691.

Yin, Z., Wang, H., Jian, M., Li, Y., Xia, K., Zhang, M., Wang, C., Wang, Q., Ma, M., and Zheng, Q.-S. (2017). Extremely black vertically aligned carbon nanotube arrays for solar steam generation. ACS Appl. Mater. Interfaces *9*, 28596–28603.

Zhu, C., Shen, H., Liu, H., Lv, X., Li, Z., and Yuan, Q. (2018). Solution-processable two-dimensional In_2Se_3 nanosheets as efficient photothermal agents for elimination of bacteria. Chem. Eur. J. *24*, 19060–19065.

iScience, Volume *24*

Supplemental Information

Remarkable bactericidal traits of a metal-ceramic composite coating elated by hierarchically structured surface

Jiang Xu, Zhijian Pan, Shaung Peng, Yanjie Zhao, Shuyun Jiang, Yu jie Chen, Zong-Han Xie, and Paul Munroe

1.Supplemental Information

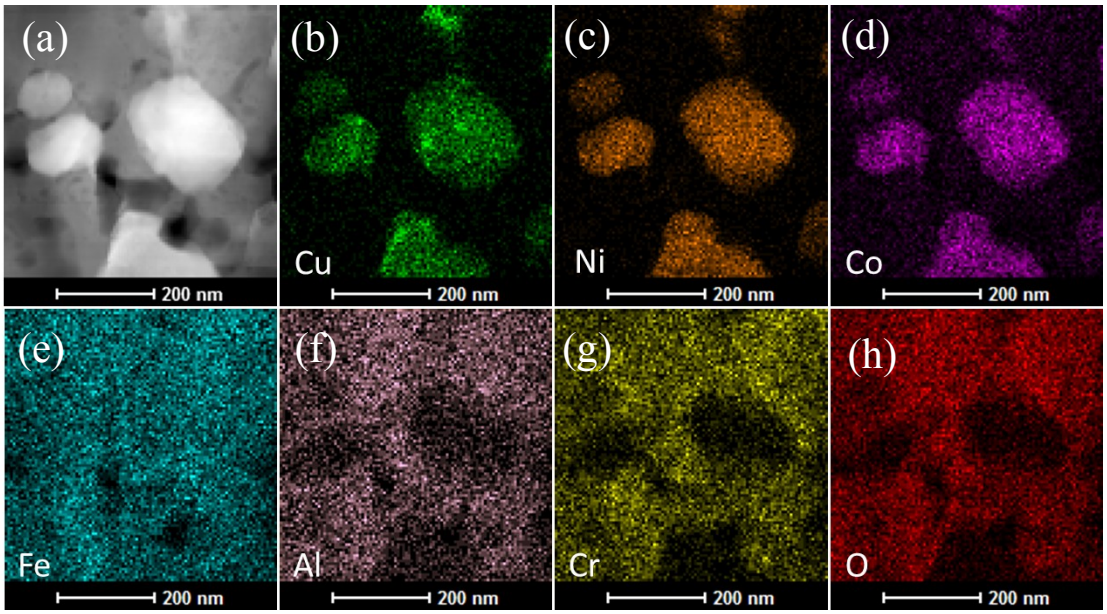

Fig. S1. STEM-EDX Elemental Maps. Related to Figure 3.
(a) Cross-sectional Z-contrast HAADF-STEM image taken from the outer-layer of the coating and the corresponding EDS elemental maps for (b) Cu, (c) Ni, (d) Co, (e) Fe, (f)Al, (g) Cr and (h) O.

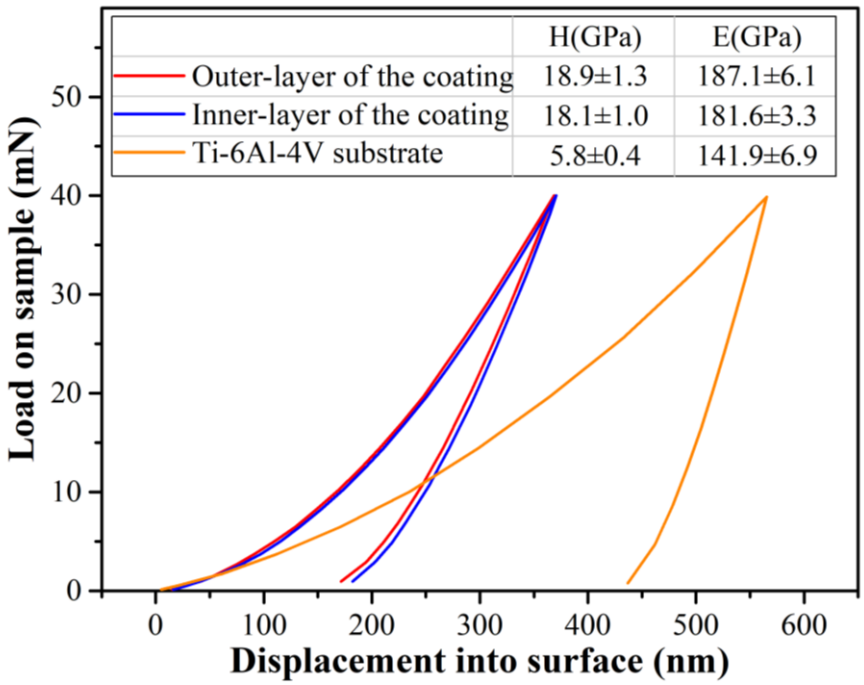

Fig. S2. The Hardness and Elastic Modulus for the uncoated Ti-6Al-4V and the Inner and Outer Layer of the Coating. Related to Figure 3.
Load–displacement curves of the outer-layer and the inner-layer of the coating, as well as uncoated Ti-6Al-4V.

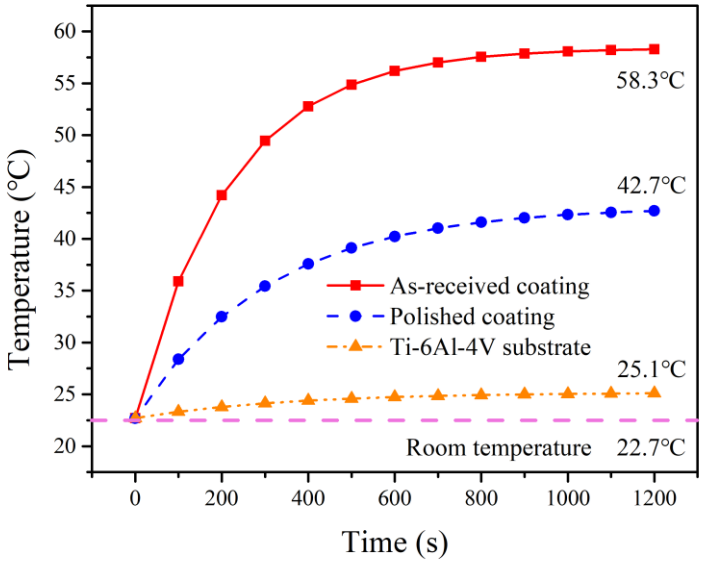

Fig. S3. The Temperature of the Bacteria Solution as a Function of Light Irradiation Time. Related to Figure 5.

The temperature of bacteria solution as a function of light irradiation time.

2. Transparent Methods

A metal-ceramic duplex phase coating was synthesized on to a Ti-6Al-4V substrate using a double-cathode glow discharge system with a self-made target material. Substrate specimens with dimensions of 20 mm×10 mm×3mm were cut from a Ti-6Al-4V rod. This target was fabricated from ball-milled Fe_2O_3 (23.49wt %), Al (7.93wt %), Cr (15.27wt %), Co (17.33 wt %), Ni (17.33 wt %) and Cu (18.65 wt %) powders by employing cold compaction under a pressure of 500 MPa. Prior to coating deposition, the background pressure of the vacuum chamber was evacuated to 5×10^{-4} Pa. The principal deposition parameters were set as follows: high-purity argon gas used as working gas maintaining the gas pressure of 35 Pa; a negative bias voltage of -300V was applied to the Ti-6Al-4V substrate; a negative bias voltage of -950V was applied to the target material; the distance between the target material and Ti-6Al-4V substrate was maintained at 10 mm; a deposition temperature and time setting of 850°C and 3.5 h, respectively, was applied.

The phase composition of the as-received coating was characterized using an X-ray diffractometer (XRD, Bruker, D8 Advance) equipped with a Cu-Kα source operating at 40 mA and 40 kV. The surface and cross-sectional morphologies for the coating were observed by a field-emission scanning electron microscope (SEM, Hitachi, S-4800, Japan) to which energy dispersive x-ray spectroscopy (EDS) facilities were attached. High-angle annular dark-field scanning transmission electron microscopy (HAADF-STEM) using an aberration-corrected FEI Titan Themis TEM operating at 200 kV was employed to analyze the microstructure of TEM samples prepared through FIB fabrication. A confocal microscope (Leica DCM8), with LeicaSCAN software, was used to observe 3-D profiles of the coating. Contact angle measurements were undertaken using a JC2000C contact angle meter at ambient temperature using a distilled water droplet with a volume of 4 μL. UV−Vis−NIR absorption spectra from the coating were acquired by using a JASCO V-670 spectrophotometer equipped with an integrating sphere accessory.

The photocatalytic activities of the as-received coating were determined by the photo-degradation of a rhodamine B (RhB) dye solution under visible light irradiation (> 420 nm) with a Xe lamp at a power density of $1W/cm^2$. The concentration of RhB solution was

calibrated against its characteristic absorption peak located at 554 nm. During the photocatalytic process, the coating samples with a radiation area of 1 mm×1 mm, which were sealed in a quartz cell, were soaked in a 3 mL RhB solution with the initial concentration of 10 mg L^{-1}. *S. aureus* (ATCC 25923) and *E. coli* (ATCC 25922) strains were selected to examine the in vitro antibacterial ability of the coating by a plate-counting method. The bacterial killing efficiencies of the coating after different exposure times under both dark and visible light conditions were quantitatively evaluated. Both gram-negative *E. coli* and gram-positive *S. aureus* were cultured in a Luria–Bertani (LB) broth under 150 rpm rotation for 24 h at 37 °C. After overnight incubation, the bacterial suspensions were centrifuged at 6000 rpm and washed twice by phosphate buffer solution (PBS) to achieve a final bacterial concentration of approximately 1×10^5 CFU mL^{-1}. Subsequently, a 100 μL bacterial suspension was placed onto the coating surface (an exposed area of 1 cm×1 cm) and incubated at 37 °C for different times under dark and visible light (using a Xe lamp at a power density of 1W/cm^2) conditions, respectively. At the end of the incubation period, each sample was rinsed in 10ml PBS and this solution was ultrasonically stirred for 5 min. The viable bacteria in the PBS were quantified by standard serial dilution and plate-counting. The bacterial suspension incubated on uncoated Ti-6Al-4V was used as a control. The antibacterial rate (R), according to the National Standard of China GB/T 21510-2008, was determined by the following expression: R=(A-B)/A×100%, where A and B are the average numbers of viable bacterial colonies (cfu/mL) on the uncoated Ti-6Al-4V (control) and the as-deposited coatings (samples), respectively. The viable bacterial were counted according to the National Standard of China GB/T 4789.2 protocol (Zhao et al., 2019). Prior to SEM observations of bacterial cells, the bacteria were fixed with 2.5% glutaraldehyde solution and then and dehydrated with 60%, 80%, 90% and 100% ethanol for 10 min each. Cu ion release tests were performed by immersing the samples with an exposed area of 1 cm ×1 cm in 10 mL of deionized water at 37 °C for 30 days. The concentrations of Cu^{2+} ions released from the as-deposited coating and the polished coating were analyzed using inductively-coupled plasma mass spectroscopy (ICP-MS, Agilent 7700, Agilent) with a detection limit of 0.2 ppb.

Supplemental References

Zhao, M., Gong, H., Ma, M., Dong, L., Huang, M., Wan, R., Gu, H., Kang, Y.andLi, D. (2019). A comparative antibacterial activity and cytocompatibility for different top layers of TiN, Ag or TiN-Ag on nanoscale TiN/Ag multilayers. Appl. Surf. Sci., 473**,** 334-342.